

Y-Mn-O 负载的 Ni 基催化剂用于乙酸自热重整产氢

胡晓敏 陈 慧 贾玄弈 王 巧 黄利宏*
(成都理工大学材料与化学化工学院, 成都 610059)

摘要: 为了有效地从生物质衍生的乙酸中获得高氢气产率, 通过水热法合成了一系列的 NiMnY 催化剂并用于乙酸自热重整 (ATR) 过程中, 并采用 X 射线衍射 (XRD)、N₂ 吸附-脱附测试、H₂ 程序升温还原 (H₂-TPR) 探究催化剂中的内在联系。在 Ni_{0.39}Mn_{0.61}YO_{3.11±δ} 催化剂中, 经焙烧后形成了类钙钛矿型 (Ni, Mn)YO₃ 物相; 经氢气还原后, 转化为含有 MnO、Y₂O₃ 和高分散 Ni 纳米粒子的热稳定的 Ni-Mn-Y-O 物种。Ni_{0.39}Mn_{0.61}YO_{3.11±δ} 具有高效稳定的产氢催化性能, 乙酸转化率达 100%, 氢气产率达到 2.68 mol_{H₂} · mol_{HAc}⁻¹。

关键词: 生物质; 非均相催化; 氢能; 镍; 钙钛矿相

中图分类号: O643.36⁺¹ 文献标识码: A 文章编号: 1001-4861(2021)03-0555-06

DOI: 10.11862/CJIC.2021.032

Y-Mn-O Supported Ni-Based Catalyst for Hydrogen Production via Auto-thermal Reforming of Acetic Acid

HU Xiao-Min CHEN Hui JIA Xuan-Yi WANG Qiao HUANG Li-Hong*

(College of Materials and Chemistry & Chemical Engineering, Chengdu University of Technology, Chengdu 610059, China)

Abstract: To effectively achieve high hydrogen yield from biomass-derived acetic acid (HAc), a series of NiMnY catalysts were prepared by hydrothermal method and tested in auto-thermal reforming (ATR) of HAc. X-ray diffraction (XRD), N₂ adsorption-desorption test and H₂-temperature-programmed reduction (H₂-TPR) were carried out to explore the internal relationship within these NiMnY catalysts. Over the Ni_{0.39}Mn_{0.61}YO_{3.11±δ} catalyst, perovskite-like (Ni, Mn)YO₃ phase was formed after calcination, and converted into thermostable Ni-Mn-Y-O species after reduction in H₂, along with the highly dispersed nickel nanoparticles. As a result, over the promoted Ni_{0.39}Mn_{0.61}YO_{3.11±δ} catalyst, a stable catalytic performance with high HAc conversion (100%) and hydrogen yield (2.68 mol_{H₂} · mol_{HAc}⁻¹) was recorded, showing potential for hydrogen production.

Keywords: biomass; heterogeneous catalysis; hydrogen energy; nickel; perovskite phases

Consumption of fossil fuel brings about environmental issues, *e. g.*, pollution and emission of greenhouse gas^[1], and alternative energies thus attract extensive attentions for decades. Among the alternative energies, hydrogen is a promising candidate for its cleanliness and high energy density^[2]. Biomass, as an abundant renewable resource, can be converted into bio-oil

via fast pyrolysis, and can be processed for hydrogen production^[3]. Acetic acid (HAc), as a main component in bio-oil with content up to mass fraction of 33%, has been selected as a feasible hydrogen resource via reforming processes^[4-5]. Within reforming processes, there are steam reforming (SR), partial oxidation (CPOX) and auto-thermal reforming (ATR), while ATR

收稿日期: 2020-09-16。收修改稿日期: 2020-12-04。

国家自然科学基金(No.21276031)、四川省科技计划项目(No.2019YFH0181)和四川省国际科技合作计划项目(No.2015HH0013)资助。

*通信联系人。E-mail: huanglihong06@cdut.cn

shows potential for its self-heat sustainability^[6-7].

In ATR of HAc ($\text{CH}_3\text{COOH} + 1.44\text{H}_2\text{O} + 0.28\text{O}_2 \rightarrow 2\text{CO}_2 + 3.44\text{H}_2$, $\Delta H = 0 \text{ kJ} \cdot \text{mol}^{-1}$), nickel-based catalysts are effective for their reactivity in breaking C—C and C—H bond within acetic acid^[8], but deactivation issues, like coking and sintering, hinder the process; for example, in Ca-Al layered double hydroxides-derived Ni-based catalysts for ATR reaction, as reported by Wang et al.^[7], the layered double hydroxides structure promotes stability of the nickel-based catalyst, but severe coking is still observed with time-on-stream. To address these issues, additives are then introduced in Ni-based catalysts to modify their structures and electronic properties. Manganese, as a transition metal, exhibits redox ability to activate oxygen species for its multi-valences and can be effective to gasify coke precursors in ATR^[9-10]. As reported by Liu et al., within a spinel Co-Mn-Ni-O catalyst, the redox cycle of $\text{Mn}^{2+}/\text{Mn}^{3+}$ and $\text{Mn}^{3+}/\text{Mn}^{4+}$ promotes the transfer of oxygen species in zinc-air batteries^[10]. However, the MnO_x is easy to be sintered which results in poor thermostability in $\text{NiMn}_{4.78}\text{O}_{7.39\pm\delta}$ catalysts, as reported by An et al.^[11-12]. To improve thermostability, yttrium can be a promising candidate^[13-14]; for example, nickel-based catalysts with yttrium oxide presents stable reactivity in partial oxidation of methane (POM) at a high temperature (850 °C)^[13-14]. Besides, with the addition of manganese into perovskite structure of ABO_3 with nickel and yttrium (NiYO_3), a perovskite-like $(\text{Ni}, \text{Mn})\text{YO}_3$ phase can

be formed, which is promising to restrain sintering and oxidation within nickel-based catalysts.

In light of above reports, a series of NiMnY catalysts were synthesized by hydrothermal method in the current work and the calcined catalysts were then tested in ATR of HAc. The characterization techniques, such as X-ray diffraction (XRD), N_2 adsorption-desorption test and H_2 -temperature-programmed reduction (H_2 -TPR), were carried out to explore the internal relationship within those NiMnY catalysts. To the best of the author's acknowledge, there is no report on the perovskite-like $(\text{Ni}, \text{Mn})\text{YO}_3$ catalysts for hydrogen production in ATR of HAc.

1 Experimental

1.1 Catalyst preparation

A series of NiMnY catalysts with mass fraction of 15% NiO were prepared by hydrothermal method. Chemicals of $\text{Y}(\text{NO}_3)_3 \cdot 6\text{H}_2\text{O}$, $\text{Mn}(\text{NO}_3)_2$ and $\text{Ni}(\text{NO}_3)_2 \cdot 6\text{H}_2\text{O}$ with stoichiometric ratios as listed in Table 1 were mixed with ethylene glycol monomethyl ether under vigorous stirring, then transferred into a teflon bottle in an oven and remained at 240 °C for 12 h. The precipitate was then collected via centrifugation, washed with deionized water and dried at 105 °C for 12 h, followed by calcined in air at 850 °C for 4 h. The obtained catalysts were named as NY, NMY1-1, NMY6-1 and NM, respectively, as listed in Table 1.

Table 1 Composition, BET (Brunauer-Emmett-Teller) specific surface areas (S_{BET}), BJH (Barrette-Joyner-Halenda) pore volume (V_{BJH}), average pore size (D_{BJH}) and particle sizes of the Ni-based catalysts as prepared

Catalyst	Molar composition	$S_{\text{BET}} / (\text{m}^2 \cdot \text{g}^{-1})$	$V_{\text{BJH}} / (\text{cm}^3 \cdot \text{g}^{-1})$	$D_{\text{BJH}} / \text{nm}$	Particle size measured by XRD ^a / nm	
					Reduced	Spent
NY	$\text{Ni}_{0.27}\text{YO}_{1.77\pm\delta}$	13	0.024	7.4	30.6	37.1
NMY1-1	$\text{Ni}_{0.39}\text{Mn}_{0.61}\text{YO}_{3.11\pm\delta}$	13	0.028	8.2	22.8	27.6
NMY6-1	$\text{Ni}_{1.25}\text{Mn}_{4.75}\text{YO}_{12.25\pm\delta}$	12	0.033	10.7	39.9	40.7
NM	$\text{Ni}_{0.21}\text{Mn}_{1.02}\text{O}_{2.25\pm\delta}$	5	0.016	12.2	31.2	32.9

^a Calculated by Ni^0 at 44.6°

1.2 Catalytic performance evaluation

150 mg of catalyst was loaded in a continuous-flow fixed-bed quartz tubing reactor and reduced in hydrogen at 700 °C for 1 h, then a mixture of HAc/ H_2O / O_2/N_2 (molar ratio of 1: 4: 0.28: 3) with GHSV (gas

hourly space velocity) of 37 260 $\text{mL} \cdot \text{g}^{-1} \cdot \text{h}^{-1}$ was introduced into the reactor for ATR test. TCD (thermal conduction detector) and FID (flame ionization detector) detectors within gas chromatography (SC-3000B, Chuanyi Instrument) were used to monitor products.

The selectivity (S_i) of carbon-containing products ($i = \text{CO}, \text{CO}_2, \text{CH}_4, \text{CH}_3\text{COCH}_3$), HAc conversion (X_{HAc}) and hydrogen yield (Y_{H_2}) were calculated by Eq. (1~3), respectively, where $F_{i,\text{in}}$ or $F_{i,\text{out}}$ is the molar flow of i species at the inlet or outlet of the reactor, $F_{\text{HAc},\text{in}}$ or $F_{\text{HAc},\text{out}}$ is the molar flow of HAc at the inlet or outlet of the reactor, n_i is the carbon stoichiometric factor between HAc and carbon-containing products. Besides, the $F_{\text{H}_2,\text{product}}$ represents the molar ratio of hydrogen in the product.

$$S_i = \frac{F_i}{n_i (F_{\text{HAc},\text{in}} - F_{\text{HAc},\text{out}})} \times 100\% \quad (1)$$

$$X_{\text{HAc}} = \frac{F_{\text{HAc},\text{in}} - F_{\text{HAc},\text{out}}}{F_{\text{HAc},\text{in}}} \times 100\% \quad (2)$$

$$Y_{\text{H}_2} = \frac{F_{\text{H}_2,\text{product}}}{F_{\text{HAc},\text{in}}} \times 100\% \quad (3)$$

1.3 Characterizations

XRD patterns were recorded via an X-ray diffractometer (Rigaku, Ultima IV) with a Cu $K\alpha$ radiation source ($\lambda = 0.15418 \text{ nm}$, 200 mA, 40 kV) from 5° to 80° . N_2 physisorption isotherms were recorded by using a JW-BK112 apparatus at -196°C . 50 mg catalyst loaded within a TP-5076 apparatus (Xianquan Instrument) was used to perform H_2 -TPR experiments in a volume fraction of 5.0% H_2/N_2 gas flow, while the signal of H_2 was collected by a TCD.

2 Results and discussion

2.1 Characterizations of calcinated catalysts

The XRD patterns for calcinated catalysts were recorded and showed in Fig.1. For NY catalyst without Mn, strong peaks of Y_2O_3 appeared and the peaks of NiO were detected as well^[15]. For NMY1-1 with Mn ($\text{Ni}_{0.39}\text{Mn}_{0.61}\text{YO}_{3.11\pm\delta}$), Y_2O_3 phase disappeared; meanwhile, there was no Mn-containing species, and perovskite peaks of NiYO_3 were found with peaks shifting to lower angles, as compared with standard NiYO_3 phase, indicating that addition of manganese stabilized the NiYO_3 phase during calcination by partly replacing nickel and could form a perovskite-like (Ni, Mn) YO_3 phase, while nickel species were highly dispersed within the perovskite structure^[16]. For the NMY6-1 with more Mn, the main phase was YMn_2O_5 , along with trace

of NiO, Mn_2O_3 and NiMn_2O_4 . Over the NM catalyst without Y, there were spinel phases $\text{NiMn}_2\text{O}_4/\text{Mn}_3\text{O}_4$ and trace of Mn_2O_3 , while no obvious peak of NiO was found.

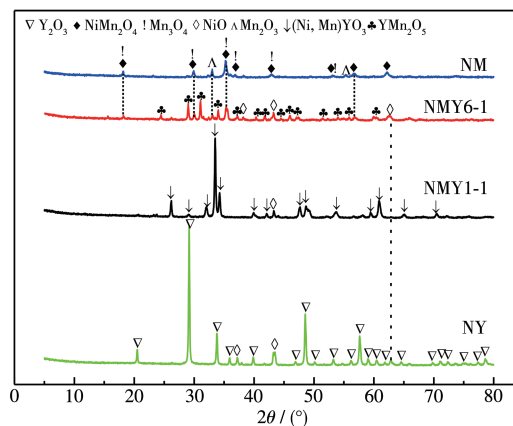


Fig.1 XRD patterns for the calcinated catalysts

The calcinated catalysts were further screened by nitrogen physisorption, as shown in Fig. 2. For the NMY1-1 catalyst, there was type II isotherm, while other three catalysts presented type III isotherms. Meanwhile, NMY1-1 showed a high specific surface area of $13 \text{ m}^2 \cdot \text{g}^{-1}$ with a concentrated pore distribution near 2 nm, as shown in Fig.2B.

2.2 Characterizations of reduced catalysts

XRD patterns of the reduced catalysts were shown in Fig.3. All catalysts presented peaks of Ni^0 ^[17]. Strong peaks of Y_2O_3 were still remained within NY catalyst. The perovskite-like (Ni, Mn) YO_3 species in NMY1-1 was transformed into Y_2O_3 and MnO, while highly dispersed Ni species with particle size near 22.8 nm was obtained, as shown in Table 1. Similar species were found in NMY6-1. For the NM catalyst, Mn_3O_4 and Mn_2O_3 were converted to MnO, and the appearance of Ni^0 can be ascribed to reduction of NiMn_2O_4 species.

Over H_2 -TPR profile of NY, the peak around 382°C was ascribed to surface NiO species, while the other one was related to NiO contacted with Y_2O_3 ^[15]. For NMY1-1, besides the weak reduction peak of surface Ni species near 374°C , a strong peak near 658°C can be attributed to reduction of (Ni, Mn) YO_3 , which is consistent with species of Ni, MnO and Y_2O_3 found by XRD^[18]. For NMY6-1, the broad peak around 490°C can be attributed to the continuous reduction of NiO,

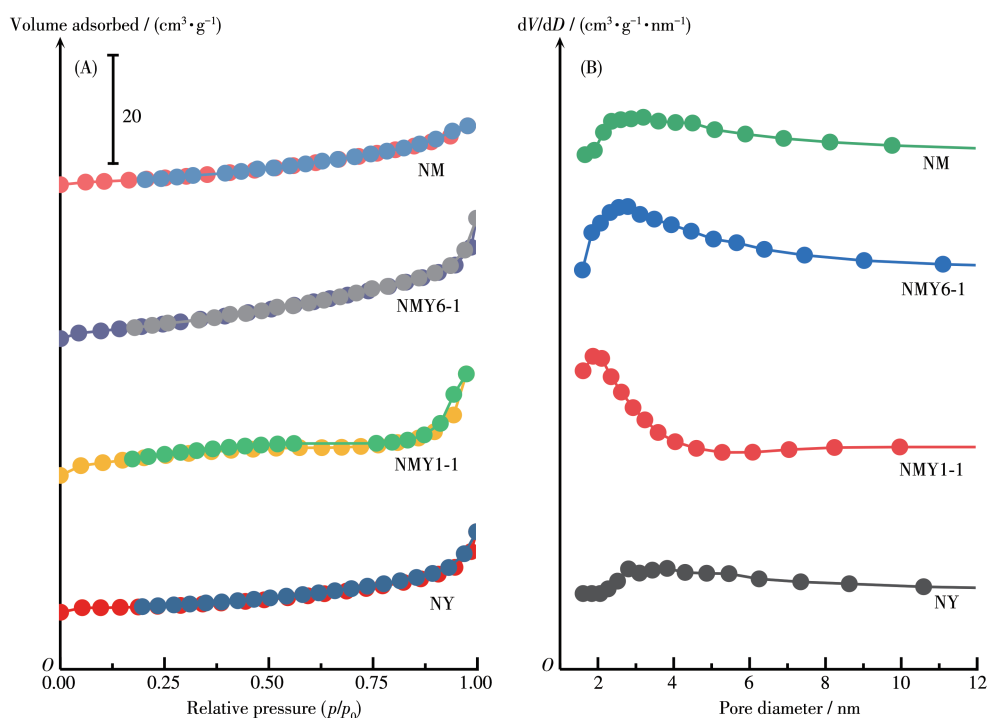


Fig.2 Adsorption-desorption equilibrium curves (A) and pore size distribution of the catalysts (B)

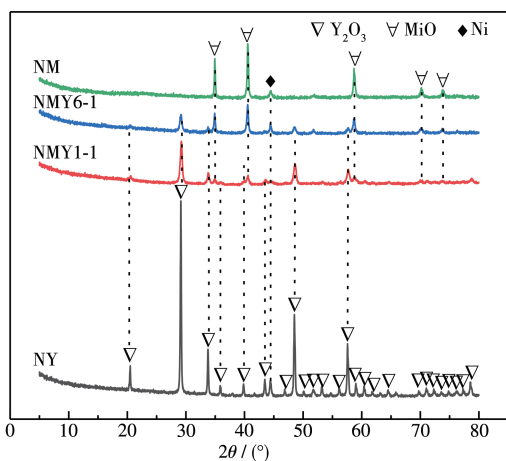


Fig.3 XRD patterns for the reduced catalysts

Mn_2O_3 and Mn_3O_4 ($\text{Mn}_2\text{O}_3 \rightarrow \text{Mn}_3\text{O}_4 \rightarrow \text{MnO}$) and the reduction of Mn^{4+} in Y_2MnO_5 ^[12,19], while the peak near 657 °C can be ascribed to the reduction of spinel ($\text{NiMn}_2\text{O}_4 \rightarrow \text{NiO} + \text{MnO} \rightarrow \text{Ni} + \text{MnO}$)^[20]. Over the NM catalyst, similar peaks were found for reduction of NiMn_2O_4 near 672 °C and species of NiO , Mn_2O_3 and Mn_3O_4 near 441 °C.

2.3 Reactivity in ATR of HAC

The catalysts were then tested in ATR of HAC at 650 °C for 20 h, as shown in Fig.5. For the NY catalyst, both HAC conversion and hydrogen yield decreased

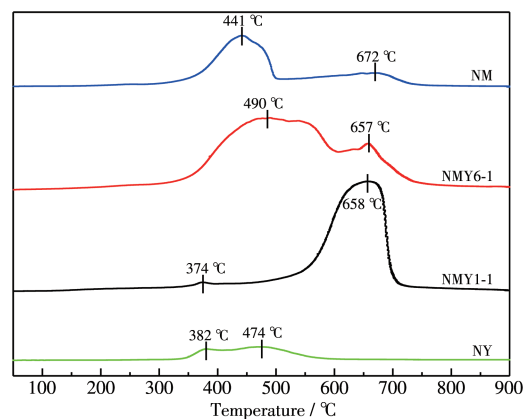


Fig.4 H_2 -TPR profile for the calcinated catalysts

overtime, and finally reached 69.6% and 1.56 $\text{mol}_{\text{H}_2} \cdot \text{mol}_{\text{HAc}}^{-1}$, respectively. For the NMY1-1, the HAC conversion remained stable near 100% with the hydrogen yield at 2.68 $\text{mol}_{\text{H}_2} \cdot \text{mol}_{\text{HAc}}^{-1}$, while only trace by-products of methane/acetone were detected and the selectivity to hydrogen was as high as 99.1%. Over the NMY6-1 catalyst, the conversion of HAC was stable at near 100%, but the hydrogen yield was near 2.50 $\text{mol}_{\text{H}_2} \cdot \text{mol}_{\text{HAc}}^{-1}$ with by-product of methane near 3.5%. In contrast, for the NM catalyst, the HAC conversion and hydrogen yield decreased to 92.3% and 2.40

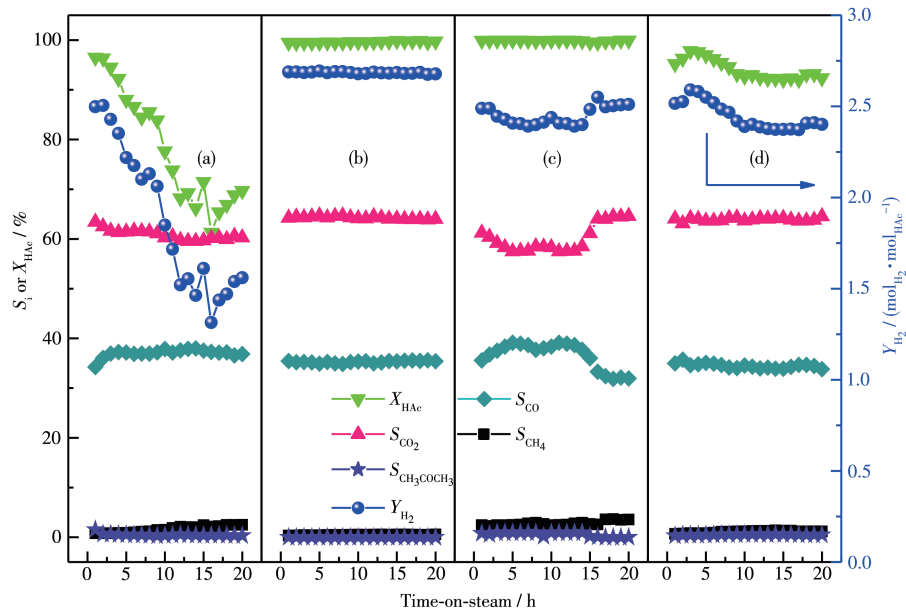


Fig.5 Reactivity of (a) NY, (b) NMY1-1, (c) NMY6-1 and (d) NM catalysts in ATR of HAC

$\text{mol}_{\text{H}_2} \cdot \text{mol}_{\text{HAc}}^{-1}$, respectively.

Effect of temperature was further estimated over the NMY1-1 catalyst, as seen in Fig.6. At 400 °C, the HAC conversion was only 48.6% with a low hydrogen yield ($0.39 \text{ mol}_{\text{H}_2} \cdot \text{mol}_{\text{HAc}}^{-1}$), while the selectivity to acetone was as high as 34.1%, indicating ketonization of HAC happened via $\text{CH}_3\text{CO}^* + \text{CH}_3^* \rightarrow \text{CH}_3\text{COCH}_3$ [15]. As the temperature went up, the hydrogen yield and HAC conversion both increased. The conversion of acetic acid reached near 100% with a high hydrogen production near $2.7 \text{ mol}_{\text{H}_2} \cdot \text{mol}_{\text{HAc}}^{-1}$ was recorded at 650 °C. However, as the temperature further increasing to 700 °C, the hydrogen production slightly decreased because of the increase of CO/CO₂ via reverse water-

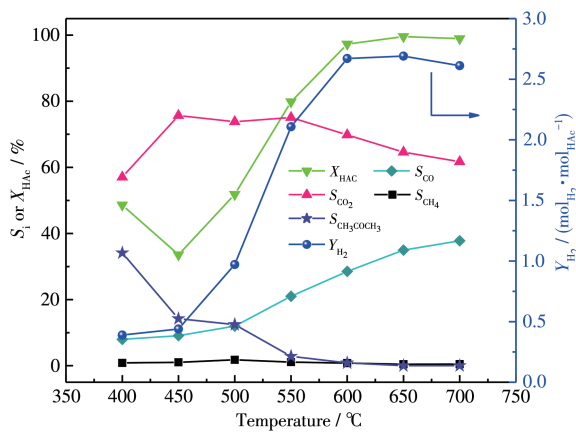


Fig.6 Effect of temperature over NMY1-1

gas shift reaction. Therefore, 650 °C can be a suitable temperature for ATR of HAC within the NMY1-1 catalyst.

2.4 Characterizations of spent catalysts

To investigate the structure variation during ATR test, XRD was carried out over the spent catalysts, as shown in Fig.7. For the spent NY catalyst, strong peaks of Y₂O₃ remained with a Ni⁰ particle size at 37.1 nm, which was slightly increased from 30.6 nm in the fresh catalyst and can be due to the weak interaction within NY. For NMY1-1, the structure phases of Ni/MnO/Y₂O₃ remained stable, and the smallest particle size at 27.6 nm for metallic nickel among these spent catalysts

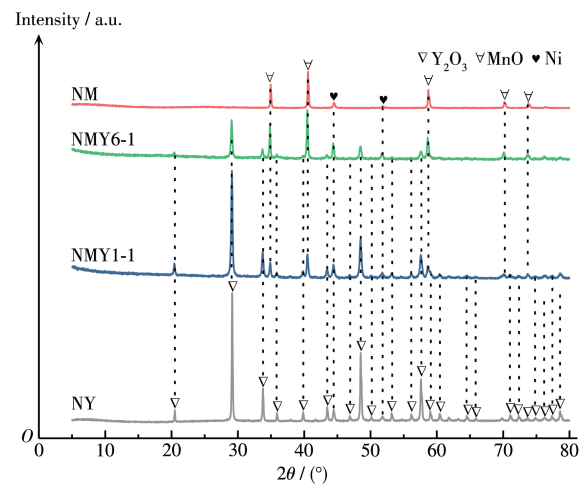


Fig.7 XRD patterns for the spent catalysts

was observed, as listed in Table 1. As compared to NMY1-1, the strength of MnO became stronger over NMY6-1, and a Ni⁰ particle size at 40.7 nm was recorded. Besides, the main phase was still MnO over spent NM catalyst, with a Ni⁰ particle size at 32.9 nm.

2.5 Discussion

In case of the NY catalyst without Mn, there was weak interaction between Ni and Y₂O₃, and during the ATR reaction, the particle size of metallic nickel increased from 30.6 to 37.1 nm, resulted in sintering and deactivation for hydrogen production. For the NMY1-1 catalyst, perovskite-like (Ni, Mn)YO₃ structure was formed and promoted dispersion of nickel species. With the addition of yttrium, the thermostability of catalyst was enhanced, while the reduction characteristic and interaction of nickel and support were tuned. After reduced in hydrogen at 700 °C, the (Ni, Mn)YO₃ transformed into thermostable species of Ni-Y-Mn-O with strong interaction among Ni, Y₂O₃ and MnO, while metallic nickel with the smallest particle size within the four catalysts (27.6 nm) was recorded; therefore, a high hydrogen yield near 2.7 mol_{H₂}·mol_{HAc}⁻¹ was obtained and remained stable without deactivation, suggesting that the Mn and Y species in (Ni, Mn)YO₃ constrained sintering and oxidation. As comparison, over NMY6-1 catalyst, a large Ni⁰ particle size near 39.9 nm was found, and a hydrogen yield near 2.5 mol_{H₂}·mol_{HAc}⁻¹ was recorded with a high selectivity to methane near 3.5% in ATR, as shown in Fig.5c. For the NM catalyst, Ni species mainly existed in spinel NiMn₂O₄ phase and were partly reduced in hydrogen at 700 °C, while a low surface area near 5 m²·g⁻¹ was found as well, resulting in less active sites to convert acetic acid and produce hydrogen, and a low hydrogen yield was then recorded near 2.4 mol_{H₂}·mol_{HAc}⁻¹.

3 Conclusions

A series of NiMnY catalysts were prepared by hydrothermal method, and tested in ATR of HAc for hydrogen production. Over NMY1-1 catalyst, the incorporation of manganese led to the formation of perovskite-like (Ni, Mn)YO₃ species, which modify the interac-

tion of (Ni, Mn)YO₃ and inhibit the sintering of nickel. Meanwhile, the addition of manganese accelerates the conversion of carbon precursor while the thermostability of catalyst is enhanced with the incorporation of yttrium. After reduction in hydrogen, the (Ni, Mn)YO₃ phase converted into MnO and Y₂O₃, along with the highly dispersed nickel nanoparticles, providing more active sites to convert HAc and generate hydrogen. Thus, a high and stable catalytic performance in ATR of HAc was obtained with HAc conversion near 100% and hydrogen yield of 2.68 mol_{H₂}·mol_{HAc}⁻¹.

References:

- [1] Meinshausen M, Meinshausen N, Hare W, Raper S C B, Frieler K, Knutti R, Frame D J, Allen M R. *Nature*, **2009**,**458**:1158-1196
- [2] Sevilla M, Mokaya R. *Energy Environ. Sci.*, **2014**,**7**:1250-1280
- [3] Zhou Q, Zhong X Y, Xie X Y, Jia X Y, Chen B Q, Wang N, Huang L H. *Renewable Energy*, **2020**,**145**:2316-2326
- [4] Li H G, Jia X Y, Wang N, Chen B Q, Xie X Y, Wang Q, Huang L H. *Appl. Catal. B*, **2020**,**267**:118370
- [5] Huber G, Iborra S, Corma A. *Chem. Rev.*, **2006**,**106**:4044-4098
- [6] Qi A D, Wang S D, Fu G Z, Wu D Y. *Appl. Catal. A*, **2005**,**293**:71-82
- [7] Wang Q, Xie W, Jia X Y, Chen B Q, An S, Xie X Y, Huang L H. *Int. J. Hydrogen Energy*, **2019**,**44**:20007-20016
- [8] Vang R T, Honkala K, Dahl S, Vestergaard E K, Schnadt J, Laegsgaard E, Clausen B S, Norskov J K. *Nat. Mater.*, **2005**,**4**:160-162
- [9] Qi K, Xie J L, Fang D, Li F X, He F. *Chin. J. Catal.*, **2017**,**38**:845-852
- [10] Wang Q, Xue Y J, Sun S S, Yan S S, Miao H, Liu Z P. *J. Power Sources*, **2019**,**435**:226761
- [11] Nagarajan N, Humadi H, Zhitomirsky I. *Electrochim. Acta*, **2006**,**51**:3039-3045
- [12] An S, Zhang Y, Hu X M, Xie X Y, Wang Q, Chen B C, Huang L H. *Fuel*, **2020**,**278**:118227
- [13] Wang Y Q, Wang W J, Hong X B, Li Y H, Zhang Z Q. *Int. J. Hydrogen Energy*, **2009**,**34**:2252-2259
- [14] Horn R, Schlögl R. *Catal. Lett.*, **2015**,**145**:23-39
- [15] Hu X M, Yang J L, Sun W J, Wang N, An S, Wang Q, Zhang Y, Xie X Y, Huang L H. *Appl. Catal. B*, **2020**,**278**:119264
- [16] Wang J J, Li G N, Li Z L, Tang C Z, Feng Z C, An H Y, Liu H L, Liu T F, Li C. *Sci. Adv.*, **2017**,**3**:e1701290
- [17] Xie W, Yang J L, Wang Q, Huang L H, Wang N. *Catal. Sci. Technol.*, **2018**,**8**:3015-3024
- [18] Baamram K, Tahir M. *Energy Convers. Manage.*, **2019**,**200**:112064
- [19] Zhang T, Li H, Yang Z, Cao F R, Li L, Chen H J, Liu H, Xiong K, Wu J, Hong Z L, Wang W C. *Appl. Catal. B*, **2019**,**247**:133-141
- [20] Ouaguenouni M H S, Benadda A, Kiennemann A, Barama A. *C. R. Chim.*, **2009**,**12**:740-747